Lowest observed surface and weld losses in fused silica fibres for gravitational wave detectors

OPEN ACCESS
IOP Publishing
Classical and Quantum Gravity
Class. Quantum Grav. **37** (2020) 195019 (19pp)
https://doi.org/10.1088/1361-6382/abac42

Lowest observed surface and weld losses in fused silica fibres for gravitational wave detectors

A V Cumming[1,3,4], B Sorazu[1,3,4], E Daw[2], G D Hammond[1], J Hough[1], R Jones[1], I W Martin[1], S Rowan[1], K A Strain[1] and D Williams[1]

[1] SUPA, Institute for Gravitational Research, School of Physics and Astronomy, University of Glasgow, Glasgow, G12 8QQ, United Kingdom
[2] Department of Physics and Astronomy, The University of Sheffield, Hicks Building, Hounsfield Road, Sheffield S3 7RH, United Kingdom

E-mail: alan.cumming@glasgow.ac.uk and borja.sorazu@glasgow.ac.uk

Received 14 May 2020, revised 22 July 2020
Accepted for publication 4 August 2020
Published 10 September 2020

Abstract

High purity fused silica has become the cornerstone choice for use in the final monolithic stage of the mirror suspensions in the gravitational wave observatories Advanced LIGO (aLIGO) and Advanced Virgo (AdV). The ultra-low thermal noise contributed by these suspensions is one of the key improvements that permitted the Nobel prize winning first direct measurement of gravitational waves in 2015. This paper outlines the first *in situ* study undertaken to analyse the thermal noise of the final monolithic stage of the aLIGO Hanford detector mirror suspensions. We analysed short operational periods of this detector, when high excitation of the transverse 'violin' modes of the silica suspension fibres occurred. This allowed detailed measurements of the Q-factor of violin modes up to order 8 of individual fibres on separate masses. We demonstrate the highest silica fibre violin mode Q-factors yet measured of up to 2×10^9. From finite element modelling, the dominant surface and weld losses have been calculated to be a factor of 3 to 4 better than previously accepted,

[3] Main authors, contributed equally to this work.
[4] Author to whom any correspondence should be addressed.

and as a result, we demonstrate that the level of noise in the aLIGO final stage silica suspensions is around 30%–40% better than previously estimated between frequencies of 10–500 Hz. This leads to an increase in the estimated event rate by a factor of 2 for aLIGO, if suspension thermal noise became the main limitation to the sensitivity of the detector.

Keywords: aLIGO, suspensions, monolithic, fused silica, mechanical loss, dissipation

(Some figures may appear in colour only in the online journal)

1. Introduction

Ground based interferometric gravitational wave detectors, including Advanced LIGO (aLIGO) [1] and Advanced Virgo (AdV) [2], are some of the most sensitive displacement measurement instruments ever built. This capability heralded the first direct measurement of gravitational waves from a binary black hole merger in 2015 [3], resulting in the 2017 Nobel Prize for physics. Since this breakthrough, the LIGO-Virgo collaboration (LVC) has now completed further data taking science runs that have yielded many subsequent gravitational wave observations including the first detection, in August 2017, of a binary neutron star merger that was accompanied by electromagnetic counterparts in the whole spectrum range [4]. To date, three science runs have been undertaken, with 11 confirmed observation during the first two runs, and 56 candidate events during the last observing run that was suspended on the 27th March 2020.

These observatories employ laser interferometry to compare changes in the length of two orthogonal 'arm' cavities, each defined by the light path between input test-mass mirrors and end test-mass mirrors. In order to achieve the levels of sensitivity required, the main optical components of the observatories must be seismically isolated. In particular, the main mirrors at the ends of both arms are suspended as multiple stage pendulums to significantly reduce seismic noise [5]. However, mechanical dissipation in these pendulum suspensions gives rise to thermal displacement noise [6], $x(\omega)$, evaluated via the fluctuation–dissipation theorem [7, 8]:

$$x(\omega) = \sqrt{\frac{4k_{\mathrm{B}}T}{m\omega}\left(\frac{{\omega_o}^2\phi(\omega)}{{\omega_o}^4\phi^2(\omega) + \left({\omega_o}^2 - \omega^2\right)^2}\right)} \tag{1}$$

where T is the temperature, m is the pendulum mass, $\phi(\omega)$ is the mechanical loss angle of the pendulum, ω_o is the resonant angular frequency, k_{B} is Boltzmann's constant and ω is the angular frequency of interest. For the suspended mirrors this noise source is significant, in particular at lower frequencies ($\sim$10–100 Hz), and therefore mechanical loss is the key material property that defines the thermal noise performance. This has resulted in the selection of high purity, ultra-low mechanical loss fused silica as the material of choice to fabricate the lowermost suspension stages [9–12].

The main mirror suspension system for aLIGO is shown in figure 1. Each observatory has four of these quadruple suspensions, two per interferometer arm, forming optical cavities for increased operational light power. The mirrors at the end of the arms are named end-test-mass mirrors, and the two input mirrors of the optical cavities named input-test mass mirrors [13]. The quadruple pendulum suspensions comprise two upper mass stages consisting of steel wires connected to blade-springs contained within metal masses. Below this, the lower pair of masses

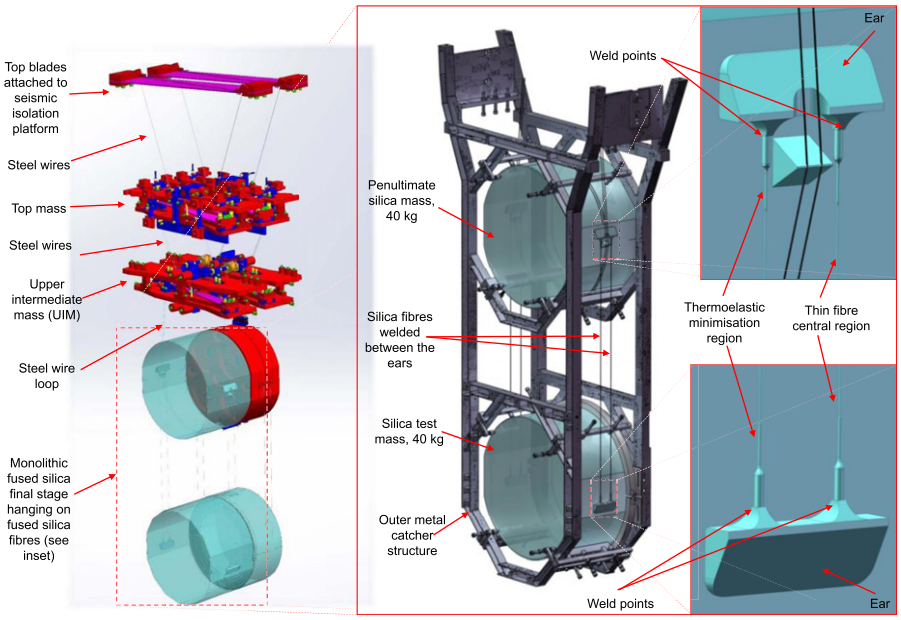

Figure 1. Quadruple suspension of the main optics for aLIGO detectors. Inset shows the last stage fused silica monolithic part of the suspension is shown which includes the main mirrors of the detectors suspended from 4 fused silica fibres. Diagram derived from [16].

are constructed in a quasi-monolithic fused silica final stage, with fused silica fibres suspending the final mass as shown in figure 1.

Suspension thermal noise results primarily from the final stage fused silica suspension fibres, and together with their attachments, known as 'ears' [16], these are therefore carefully engineered to minimise mechanical dissipation effects. This includes specific shaping of the fibre ends, to minimise thermoelastic loss associated with heat flow in the fibre as it bends [14–16]; careful choice of the central diameter of the fibre to place resonant internal modes of the fibres at appropriate frequencies [13, 17]; and high quality CO_2 laser polishing and welding of the fibres to ears to maximise strength and minimise dissipation. This means that the primary contributors, in order of significance, to the final dissipation in the system are the surface loss of the fibre, the weld loss in the attachment region and the bulk loss from the internal friction of the fibre material itself. Some residual thermoelastic loss is also present from unavoidable elastic energy that resides outwith the specifically shaped fibre ends [18].

With significant data taking periods through the first and second aLIGO observing runs, there has been the opportunity to analyse the thermal noise performance of a working suspension in the Hanford aLIGO detector. This has allowed a study to be undertaken, quantifying the magnitude of mechanical loss, particularly surface and weld loss, to a new depth in comparison to previous work [16]. As detailed in previous publications [16, 18], thermal noise performance can be estimated by measurement of the mechanical loss of the system at different frequencies. The most accessible way of estimating the mechanical loss of the silica without interference from other noise sources, is via observation of excitation of the transverse modes of vibration of the suspension fibres known as 'violin modes'. The component of the vibration along the sensitive axis of the interferometer leads to motion of the mass that is sensed by the

interferometer. This motion is of reduced amplitude due to the large inertia of the lowermost 40 kg mass. However, motion of an excited violin mode can still be easily observed in the interferometer's output signal, not only for the fundamental mode, but also for a large number of higher order harmonics. By measuring the amplitude envelope decay ('ringdown') of an array of excited modes, which exhibit damped harmonic motion, the mechanical loss can be determined from the Q-factor, $Q(\omega_o)$, of the resonance, where:

$$Q(\omega_o) = \frac{1}{\phi(\omega_o)}. \tag{2}$$

Results of these measurements are the subject of this paper, where we shall demonstrate the lowest measured losses to date on violin modes in aLIGO suspensions. Violin modes provide a unique and accessible vehicle for extracting properties about the fused silica fibres. By contrast, measurement of the pendulum mode is extremely difficult as an excessively excited pendulum mode would knock the detector out of lock (or be damped by the interferometer's active control), and would require excessively long periods of time to perform the Q measurement. From these measured losses, we were able to re-evaluate the loss components of the fused silica material that contribute to the dissipation, by comparison to established detailed finite element analysis (FEA) models (as will be detailed in section 4) to accurately describe the energy distributions in the suspension elements. Specifically, the analysis showed that dissipation due to surface and weld losses in fused silica suspension fibres are significantly lower than previously measured. From these new mechanical losses the projected thermal noise of the suspension could be recalculated using the fluctuation dissipation theorem. The primary contribution to this noise is the horizontal pendulum mode noise, with small additional contributions from the vertical and violin modes around their resonances. This recalculation was undertaken for each individual resonant mode of the suspension, calculated from first principles using the new surface and weld loss values. These were summed in quadrature to give a final projected noise.

Refining the knowledge of these properties of silica is also important for characterisation of the next stage upgrade of aLIGO, known as A+ [19], which will employ thinner suspension fibres for further improvement in performance. Furthermore, this technique will be crucial to future generations of detectors currently under design that will potentially implement large scale silica suspensions, including Einstein Telescope's high frequency (ET HF) interferometers [20], and LIGO's possible future detector, Cosmic Explorer [21].

2. Violin mode *Q*-factor measurement technique

Typically, violin modes are not excessively excited during the normal operation of the detectors. However, during certain time periods the observatory had been operating in a low noise state for tens of hours while the violin modes were particularly excited due to unusual seismic events. This gave a unique opportunity to measure the respective modes Q values, and therefore their mechanical losses for up to the eighth harmonic. The violin mode motion that resulted from the excitations can be seen in the interferometer's output signal, as the final mirror has a small percentage of the violin mode's motion imparted into it. This is quantified by the coupling term $\frac{2m_{\text{fibre}}}{\pi^2 m\nu^2}$ in the equation for thermal noise of the jth individual violin mode, derived from equation (1) [22]:

$$x_{\text{violin }j}(\omega) = \sqrt{\frac{4k_BT}{m\omega}\frac{2m_{\text{fibre}}}{\pi^2 m\nu^2}\left(\frac{\omega_{\text{violin }j}{}^2\phi_{\text{violin }j}(\omega)}{\omega_{\text{violin }j}{}^4\phi_{\text{violin }j}{}^2(\omega) + \left(\omega_{\text{violin }j}{}^2 - \omega^2\right)^2}\right)} \tag{3}$$

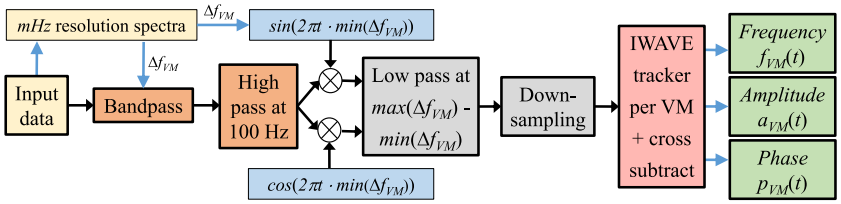

Figure 2. Block diagram of the algorithm used to monitor frequency, amplitude and phase of the violin modes of the monolithic suspensions in aLIGO. $\Delta f_{\rm VM}$ represents the frequency range of the violin modes for a given harmonic. IWAVE is the main digital tracking algorithm configured as a digital PLL that locks to the tracked line in real-time. One individual tracker is run for each individual violin mode. A cross-subtraction technique was implemented to reduce cross contamination due to the proximity of the modes. The output is the simultaneous dynamic tracking of amplitude, phase and frequency of the oscillations of individual violin modes.

where, $m_{\rm fibre}$ is the mass of each fibre, $\omega_{\rm violin\,j}$ is the respective violin resonant mode frequency, v is the respective violin mode number, and $\phi_{\rm violin\,j}(\omega)$ is the total loss for the respective violin mode. In aLIGO the ratio $\frac{m}{m_{\rm fibre}}$ is $\sim$250 000. Therefore, large excitation of the violin modes is required to produce motion of the test mass mirror significant enough to be easily measured. In fact, in order to reduce their excitation during science operation of the interferometer, active damping of all suspension fibre violin modes of $v = 1$ and 2 is typically applied locally to each main optic suspension. For the current study we chose times when this active damping was specifically turned off.

Violin modes of suspension fibres have been shown to have extremely high Q-factors [16]. For each individual fibre, two resonances for each mode number v are present, these being oscillation of the respective mode shape in two orthogonal physical directions. Orthogonal modes are typically split in frequency (due to mechanical asymmetries) by 0.1 Hz, making monitoring of individual split modes an experimental challenge. Moreover, the repeatability of the fibre manufacture and the welding process causes equivalent resonances of different respective fibres on a given suspension to also have small spread in frequency (typically 1–2 Hz). Keeping this spread in frequencies small was an important initial requirement for the fibres to reduce the amount of the detection band where the violin mode resonant peaks intrude. Thus, for a four fibre mirror suspension up to eight individual violin modes (2 orthogonal modes per fibre) of a given mode number v can be measured. In this study, modes from $v = 1$ to 8 were investigated, yielding a total of 64 possible measurements per mirror suspension.

The very close proximity of the frequencies of both split orthogonal modes, and separate fibres therefore make it difficult to monitor each mode separately. The algorithm used to accomplish this consist of 5 stages as described by figure 2. Firstly, a high resolution spectrum (mHz resolution) of the input data at the beginning of the data segment of interest was generated. This step provided an initial estimation of the violin mode frequencies for all the tracked harmonics with frequencies ranging from 500 Hz to almost 4 kHz. Secondly, a digital elliptic bandpass IIR filter [23] was applied to only allow through the frequencies of the violin modes of each harmonic order being tracked. The equiripple behaviour of these type of filters, allows a minimum stop-band attenuation to be specified with the fastest transition in gain between passband and stopband for a given filter order and amount of ripple. A bandpass ripple of 0.5 dB was allowed as it did not introduce noticeable perturbations of the amplitude of the violin mode being tracked. The stopband attenuation changed between 40 and 70 dB depending on the harmonic order of the violin mode being tracked, with bandpass ranging from a few tens of

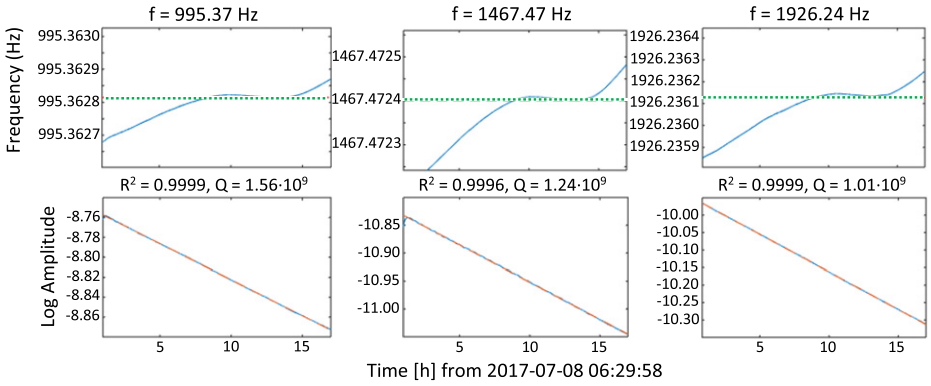

Figure 3. Q-factor measurement of individual 2nd (left), 3rd (middle horizontally) and 4th (right) harmonics of violin modes associated with the LHO ITMX suspension. (Top row) Represents the tracked frequency in blue with the median in green (Bottom row) Logarithmic ring down of their excited amplitude in blue with the linear fit in red—R^2 is the goodness of fit, and measured Q for each shown above the plot.

Hertz to 100 Hz. A first order Butterworth high pass filter was also applied to further attenuate dominant low frequency noise below 100 Hz. Thirdly, the filtered data was heterodyned to a frequency 10 Hz below the minimum violin mode frequency of the harmonic being tracked. Both quadratures were generated by multiplying the data by a sine and cosine wave at the appropriate heterodyne frequency. Fourthly, a low pass equiripple filter of 70 dB attenuation was applied to both heterodyned quadratures with the cutoff frequency being 10 Hz above the maximum violin mode frequency of the harmonic being tracked. This was sufficient to down-sample the data without aliasing. The data rate was reduced from an input data sampling rate of 16 kHz to just a few hundred Hz. This step was necessary to reduce the computing power required by the line tracking algorithm.

From the several digital tracking algorithms tested, IWAVE [24, to be published] was the most successful in separating the very high Q violin modes with very similar frequencies. This algorithm is based on a dynamic infinite impulse response IIR filter of complex coefficients with a transfer function that resembles a damped oscillator of controllable frequency and quality factor. The implementation of this algorithm for violin mode monitoring was to configure it as a digital phased-locked loop (PLL) that locked to each violin mode in real-time, providing simultaneous independent dynamic tracking of amplitude, frequency and phase of individual violin modes. One independent IWAVE line tracker was run per individual violin mode frequency for each harmonic being analysed. Cross contamination of nearby high Q modes was reduced by implementation of a cross-subtraction technique, such that, before feeding the input data to each IWAVE tracker, we subtract the outputs for all the other trackers from the input. The input data to the violin mode monitoring algorithm is the output raw data of the LIGO Hanford detector.

The frequencies, amplitudes and phase variations of all violin modes up to order $\nu = 8$ for the input test mass suspension of the interferometer's 'x' arm (ITMX) at the aLIGO Hanford observatory (LHO) were tracked. This suspension was chosen because it was the one of the most comprehensively characterised suspensions in terms of fibre weld positioning, fibre break off positions, all measured from high resolution photographs.

In order to identify which violin mode frequencies are associated to the ITMX suspension being analysed, two approaches were taken. The fundamental violin modes and low order

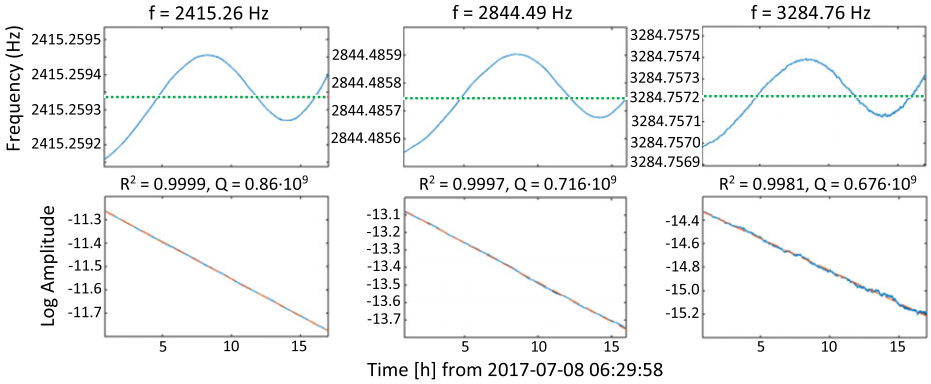

Figure 4. Q-factor measurement of individual 5th (left), 6th (middle horizontally) and 7th (right) harmonics of violin modes associated with the LHO ITMY suspension. (Top row) Represents the tracked frequency in blue with the median in green (Bottom row) logarithmic ring down of their excited amplitude in blue with the linear fit in red—R^2 is the goodness of fit, and measured Q for each shown above the plot.

harmonics were identified by driving each suspension individually and looking which modes were being excited. This method was not effective to identify higher order harmonics as the amplitude of the excitation decreases with increasing frequency. In addition, this invasive method has a negative impact on the duty cycle of the detectors. In order to identify the violin mode frequencies of the higher order harmonics associated with each individual suspension, a non-invasive method was developed. This method consisted of looking at the time fluctuations of the frequency and phase outputs of the line trackers locked to each individual violin mode frequency. Patterns in the time fluctuations can be identified for the fibres associated with each suspension. These fluctuations are, most probably, associated with local thermal fluctuations around the fibres. The thermal fluctuations cause changes in the length of the fibre based on thermal expansion, but mainly by Young's modulus dependency with temperature. We observed that temperature changes of about 0.05 degrees caused changes in the fundamental mode frequency of $\sim$50 μHz. Figures 3 and 4 show an example of the line tracker outputs when analysing 3 violin mode harmonics of two different suspensions. The top row shows the variation in time of the frequency output of each tracked violin mode. This information was used to identify each violin mode with a suspension as described above. For clarity, we do not show the phase output of the line trackers, however it is the combined information of the variation in time of the phase and frequency outputs that provide a powerful technique for identifying the violin modes of higher order harmonics to their suspensions, as will be shown in another publication. In figure 3 we show the tracking results of violin mode measurements of 2nd, 3rd and 4th harmonics of individual fibres belonging to the ITMX mirror suspension. By contrast, figure 4 shows violin modes for the 5th, 6th and 7th harmonics of fibres belonging to the 'y' arm's input mirror suspension (ITMY), measured during the same time interval as those in figure 3. The time fluctuation variations of the frequency outputs are very similar for all the violin mode harmonics associated with fibres of one single mirror suspension. However, a different pattern can clearly be seen for fibres associated with a different mirror suspension.

The respective modes ring down are also shown in the middle rows of figures 3 and 4, as logarithmic plots of the oscillation amplitude. A linear fit was then applied to each logarithmic

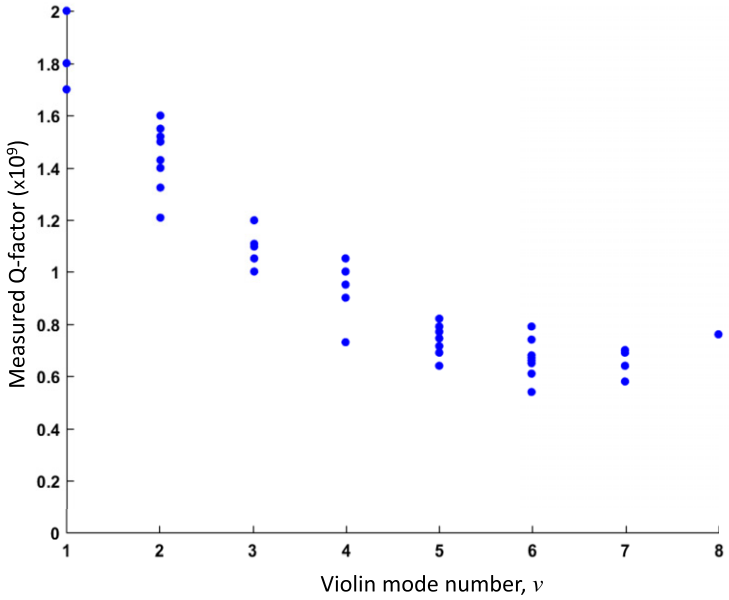

Figure 5. Q-factor measured from the ring down of individually excited fibres of violin mode numbers $v = 1$ to 8 of the ITMX monolithic suspension at the aLIGO Hanford observatory.

ringdown with the red dashed line representing the fit line of each ringdown. The Q-factor is calculated from the slope of the fitted line, s, as:

$$Q(f_o) = \frac{1}{\phi(f_o)} = \frac{\pi \cdot f_0}{s} \tag{4}$$

where f_0 is the median of the tracked frequency.

Ringdown measurements of different modes were recorded during two different long segments of continuous lock with the detectors operating in science mode (therefore low noise operation). By using a single lock acquisition, with no lock losses on each long data segment, a single excitation of the suspension fibres' violin modes was able to be monitored, giving a more accurate fit to each single long ringdown. The two segments used are of 36 h (from 2015-12-19 07:00:00 UTC) and 17 h (from 2017-07-08 06:30:00 UTC), the latter being 2 days after a significant magnitude 7.1 earthquake [25] near Washington state, that considerably excited the detector suspensions, driving the higher order violin modes to a high enough amplitude to be able to measure their Q values. Data segments of a minimum of 17 h were analysed to obtain violin mode ring downs. These data gave ability to measure a good proportion of the $1/e$ decay time each ring down.

3. Measured *Q*-factor results of violin modes for ITMX mirror suspension

Figure 5 shows the compiled results of all the measured violin mode Q-factor values for individual fibres with mode numbers $v = 1$ to 8 associated with the fibres of the LHO ITMX suspension. Modes of $v > 8$ were not sufficiently excited to produce useful measurements. For some of the harmonics, it was not possible to measure all of the potential eight modes per

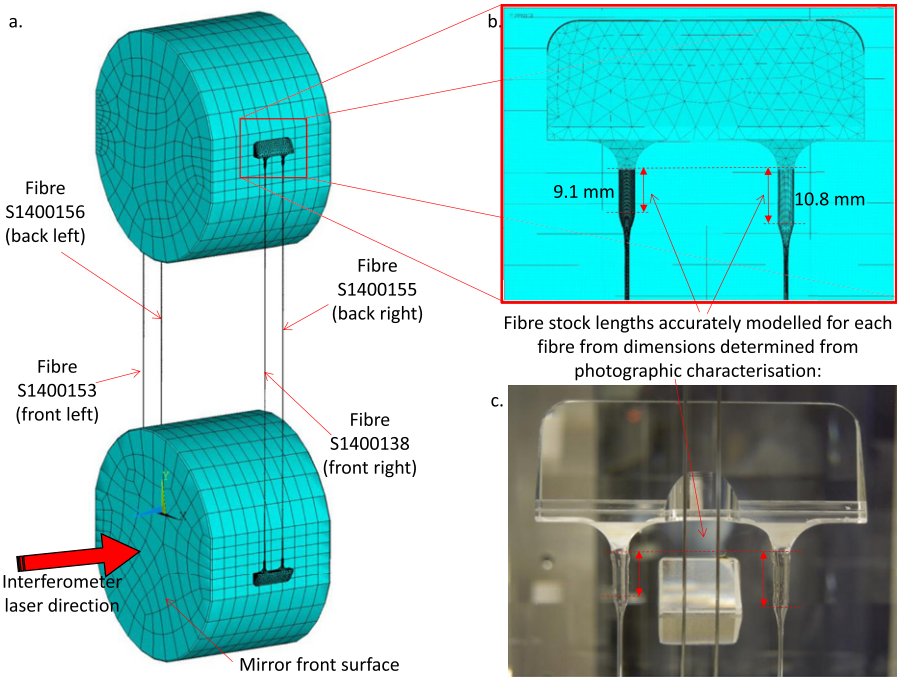

Figure 6. (a) FEA model of the aLIGO Hanford ITMX monolithic fused silica suspension stage, showing fibre serial numbers and their locations (b) inset showing fibres on one ear, with fibre vertical positions derived from measurements of photograph shown in inset (c). The prism and wires used to suspend from upper stage shown in inset c. are omitted from the FEA model, as they do not alter the observed violin modes or energy distributions.

harmonic, as explained in section 2, particularly at higher mode numbers where excitation is lower. Also, it is likely that some modes would move the test mass optic perpendicular to the measurement axis of the interferometer, meaning they would not be easily sensed.

The Q-factors shown in figure 5 are the highest ever measured to date for any fused silica gravitational wave observatory suspension, showing a factor of 2.7–3.2 greater than those measured on the prototype suspension at MIT [16] for the fundamental and second order modes. These results show the high resulting quality of the production suspensions that facilitated the ground breaking gravitational wave detections in 2015 and beyond. The results show the expected trend of fall off in measured Q value as mode number increases, this being well known from previous studies [26], and results from increasing levels of energy held towards the more lossy ends of the fibre as mode number increases. This trend in the measurements allows a re-analysis of the material properties of fused silica, and the resulting predicted thermal noise, as shall now be demonstrated.

4. FEA model, and predicted losses

For comparison with the measured violin mode loss values (inverse of the Q-factor values shown in figure 5), a detailed FEA model was constructed of the ITMX suspension. This based on the principles outlined in [16, 18, 27], where the fibre shape is carefully meshed in element slices through its cross section to allow amenable calculation of surface and thermoelastic loss.

The model composed of 4 independent fibres, as shown in figure 6, and was built in FEA using geometries taken from the detailed inspection profiles taken on the apparatus described in [28] as part of the fibre qualification process prior to detector installation. This is an extension of the technique outlined in [16], which used 4 identical fibre profiles. Additional care was placed on ensuring the correct vertical positioning of the fibres and therefore of their bending points, by measurement of the exact lengths of the fibres via high-resolution photographs of the final installation of the suspensions. These were taken as part of final qualification process, as shown in figure 6(c), something not available on early prototype work undertaken in previous studies [16, 18, 23].

The FEA model allows a detailed elastic energy analysis to quantify the energy distribution throughout the suspension. The mechanical loss of the fibre was modelled as the sum of loss components—the frequency-dependent loss $\phi_{\text{bulk}}(\omega)$ associated with the bulk material making up the fibre, a frequency-independent component from loss arising at the fibre surface ϕ_{surface} and a frequency-dependent thermoelastic loss component, $\phi_{\text{thermoelastic}}(\omega)$. Additionally, there is known loss in the weld area of the fibre, $\phi_{\text{weld.}}$ The total mechanical loss of the fibre's material was predicted using the FEA model's energy distribution to weight each element of the model's mechanical loss contribution, E_i, to the total, $E_{\text{elastic total}}$, this technique being well established and explained in detail in [16, 18, 23]:

$$\phi_{\text{fibre}}(\omega) = \sum_{i=1}^{n} \frac{E_i}{E_{\text{elastic total}}} \left(\phi_{\text{thermoelastic}}(\omega) + \phi_{\text{surface}} + \phi_{\text{bulk}}(\omega)\right) + \frac{E_{\text{welds}}}{E_{\text{elastic total}}} \phi_{\text{weld}}. \tag{5}$$

where E_{welds} is the total energy contained in the weld material.

Thermoelastic loss in the *i*th element is given by [14]:

$$\phi_{\text{thermoelastic}}(\omega) = \frac{YT}{\rho C}\left(\alpha - \sigma_i \frac{\beta}{Y}\right)^2 \frac{\omega\tau_i}{1 + (\omega\tau_i)^2} \tag{6}$$

where τ_i is the characteristic heat flow time over the elemental slice through the fibre [18, 27], T is temperature, ρ is the density, C is the specific heat capacity, α is the coefficient of linear thermal expansion, σ_i is the static stress in the *i*th element, Y is Young's modulus and $\beta = \frac{1}{Y}\frac{\mathrm{d}Y}{\mathrm{d}T}$ is the thermal elastic coefficient. All parameters used to calculate thermoelastic loss are well quantified. By contrast, surface loss in the *i*th element is given by [29]:

$$\phi_{\text{surface}} = \frac{8h\phi_s}{d_i} \tag{7}$$

where $h\phi_s$ is the product of the mechanical loss of the material surface, ϕ_s, and the depth, h, over which surface loss mechanisms are believed to occur, where d_i is the average diameter of the *i*th element along the fibre length. A value of 6.15×10^{-12} m has traditionally been taken from Gretarsson and Harry for $h\phi_s$ [29], however some laboratory evidence exists [30, 31] to suggest that the true value may in fact be lower. As such, comparison of the actual Q-factors measured in this work to the mechanical losses predicted through the FEA modelling, allows this value to be re-evaluated.

Bulk loss is given by:

$$\phi_{\text{bulk}}(\omega) = C_2 \left(\frac{\omega}{2\pi}\right)^{0.77} \tag{8}$$

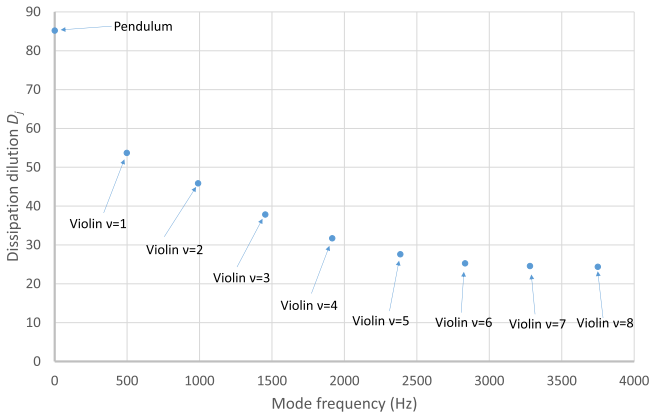

Mode	Dissipation dilution D_j
Pendulum	85
Violin mode v=1	54
Violin mode v=2	46
Violin mode v=3	38
Violin mode v=4	32
Violin mode v=5	28
Violin mode v=6	25
Violin mode v=7	25
Violin mode v=8	24

Figure 7. Dissipation dilution values used in the analysis, showing pendulum and first 8 violin modes.

where C_2 is an empirically evaluated constant as in Penn *et al* [32]. For the fibre material, Suprasil 2, its value is $1.18 \pm 0.04 \times 10^{-11}$. The error on this value is small, and the bulk loss has been shown not to be a dominant loss term for thin fibres [18, 23], so the value of C_2 was not re-evaluated here.

ϕ_{weld} is the material loss of the volume of material that has been re-heated to form the welded joint at the ends of the fibre. This loss is greater than that of equivalent silica as demonstrated in experimental work by Heptonstall *et al* [33], and therefore its loss is evaluated using an experimentally measured value, as parameters such as $h\phi_s$ for weld material are not explicitly known. This has previously conservatively been taken as 5.8×10^{-7} from [33], which provides a relatively large range of weld loss values from $3.2 \pm 1.8 \times 10^{-7}$ to $1.8 \pm 0.3 \times 10^{-6}$. This range of values is close to an order of magnitude, therefore a refined estimation is possible by comparison with the measured Q-factor values on the real production suspension.

In order to compare the measured Q-factor, $Q_{\text{violin}\,j}$, of the jth violin mode, we need also to include the dissipation dilution of the jth mode in equation (5):

$$\begin{aligned}\frac{1}{Q_{\text{violin }\,j}} &= \phi_{\text{violin }\,j}(\omega) \\ &= \frac{1}{D_j}\left(\sum_{i=1}^{n}\frac{E_i}{E_{\text{elastic total }\,j}}\left(\phi_{\text{thermoelastic}}(\omega)+\phi_{\text{surface}}+\phi_{\text{bulk}}(\omega)\right)\right. \\ &\quad \left.+\frac{E_{\text{welds}}}{E_{\text{elastic total }\,j}}\phi_{\text{welds}}\right). \end{aligned} \tag{9}$$

The dissipation dilution results from a significant portion of the energy of the system being stored in the lossless local gravitational field, and for the respective resonant mode, D_j, evaluated using FEA energy distribution totals, as in [18, 34]:

$$\frac{1}{D_j} = \frac{E_{\text{kinetic total }\,j}}{E_{\text{elastic total }\,j}} \tag{10}$$

The dissipation dilution values, D_j, evaluated from FEA and used in the analysis are shown in figure 7.

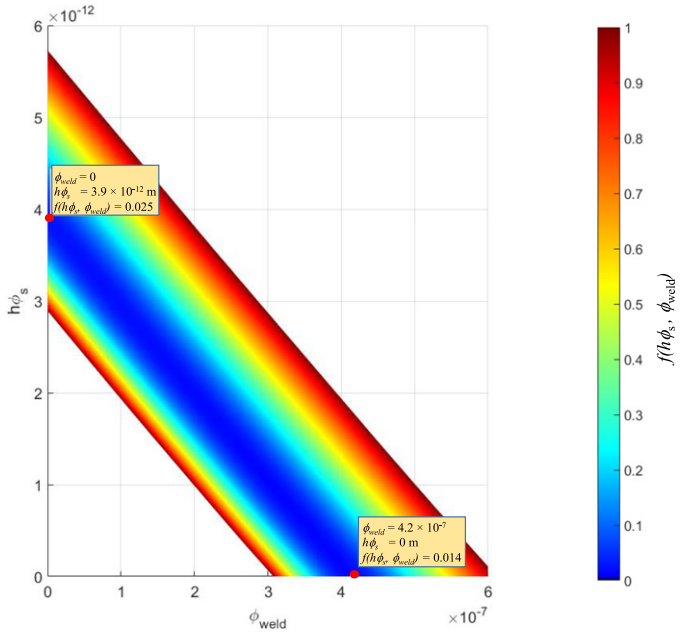

Figure 8. Contour plot of error function $f(h\phi_s, \phi_{\text{weld}})$ estimated over a wide range of values of the parameter space $(h\phi_s, \phi_{\text{weld}})$, with lowest values (blue) indicating best fit to experimental data. Highlighted data points, show the end points of the trough, with respective extreme values for $h\phi_s$ when $\phi_{\text{weld}} = 0$, and ϕ_{weld} when $h\phi_s = 0$. Values of $f(h\phi_s, \phi_{\text{weld}})$ greater than 1 have been omitted for clarity.

Equation (9) allows us to compare the measured data, $Q_{\text{violin}\,j}$, to the calculated FEA data, allowing the parameters $h\phi_s$ and ϕ_{weld} to vary and be optimised to fit the measured data, as shall now be discussed.

5. Fitting of modelled *Q*-factors to measurements, to extract surface and weld loss

By combining the array of measured Q-factor values with the accurate FEA suspension model, it has been possible to re-analyse the surface and weld loss in the installed suspension fibres. These suspensions have been hanging for extended periods of time, and were produced via what is now a highly mature production technique.

The new estimated values of the surface and weld loss parameters were extracted by the comparison and minimization of the differences between the experimental mechanical loss values and the values predicted using the calculations from FEA simulations described in section 4. The error function to be minimized as a function of the surface and weld loss $f(h\phi_s, \phi_{\text{weld}})$ is given by the non-linear least square function of the sum of the squares of the difference between the FEA estimated $\phi_{\text{violin}\,k}\,(h\phi_s, \phi_{\text{weld}})$ and the experimental measurements mechanical loss ϕ_k, for all the violin mode harmonics, k:

$$f\,(h\phi_s, \phi_{\text{weld}}) = \sum_{k=1}^{N} (\phi_{\text{violin}\;k}\,(h\phi_s, \phi_{\text{weld}}) - \phi_k)^2. \tag{11}$$

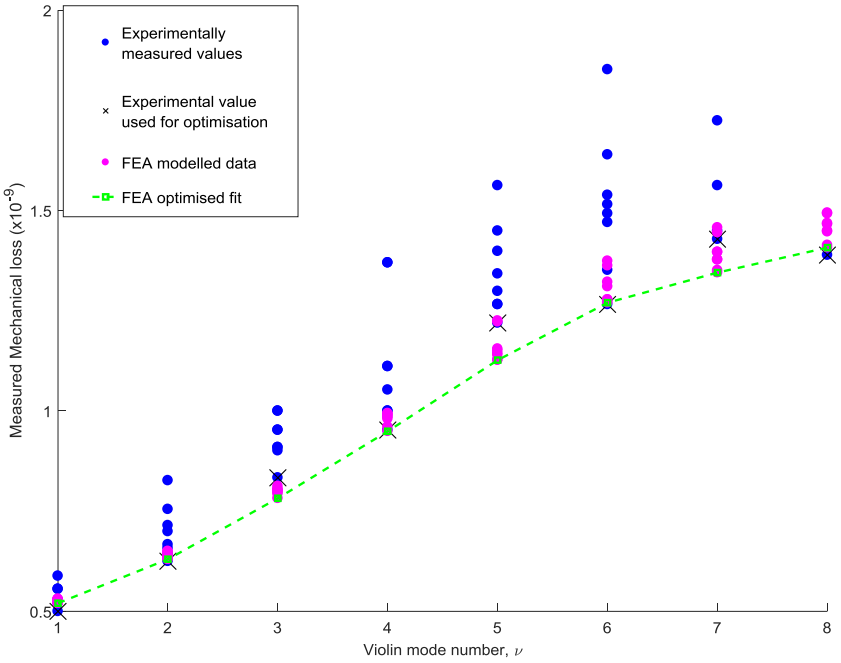

Figure 9. Fit of FEA modelled data to measured data, setting $\phi_{\text{weld}} = 1.4 \times 10^{-7}$, giving $h\phi_s$ fit of 2.5×10^{-12} m. The green points show the FEA modelled data for this chosen weld loss and the green line is shown as an aid to the eye for the fitted points. Measured data in blue are the same as shown in figure 5 and expressed as mechanical loss instead of Q-factor.

No weighting factors were applied to the error function, as there are no apparent physical mechanisms that would favour one harmonic's measured values to be more significant than those from other harmonics, therefore all experimental data points contributed equally to the error function. Fitting is done to the highest measured Q values per harmonic, to give the most clear estimation of the $h\phi_s$, ϕ_{weld} values of fused silica and therefore the material's true capabilities. The slightly lower Q's measured in the spread per harmonic are likely to have small amounts of additional dissipation potentially coming from other small energy leakages, for example into upper stages, this being an area of continuing study. A contour plot of the error function $f(h\phi_s, \phi_{\text{weld}})$ estimated over a wide range of values of the parameter space ($h\phi_s$, ϕ_{weld}) is shown in figure 8.

A clear trough shape to this surface is apparent, with the lowest points in the trough being where the error function is minimised, indicating a good fit between the experimental data and the model. This region places absolute limits on the maximum possible values for $h\phi_s$ and ϕ_{weld}. From figure 8, we see that in the extreme case of assumption that all loss is contributed only by surface, bulk and residual thermoelastic, namely when $\phi_{\text{weld}} = 0$, then the surface loss term is $h\phi_s = 3.9 \times 10^{-12}$ m. This is the maximal value for $h\phi_s$ as it essentially assumes that all the dissipation in the system occurs from this loss mechanism (ϕ_{bulk} and $\phi_{\text{thermoelastic}}$ being small by comparison). Similarly, in the extreme case where we assume that all loss is contributed only by weld, bulk and residual thermoelastic, namely when $h\phi_s = 0$ m, then the weld loss term is seen to be $\phi_{\text{weld}} = 4.2 \times 10^{-7}$.

These values are important as they place hard upper limits on $h\phi_s$ and ϕ_{weld} based on the measured values, and those upper limits are notably lower than the previously accepted values,

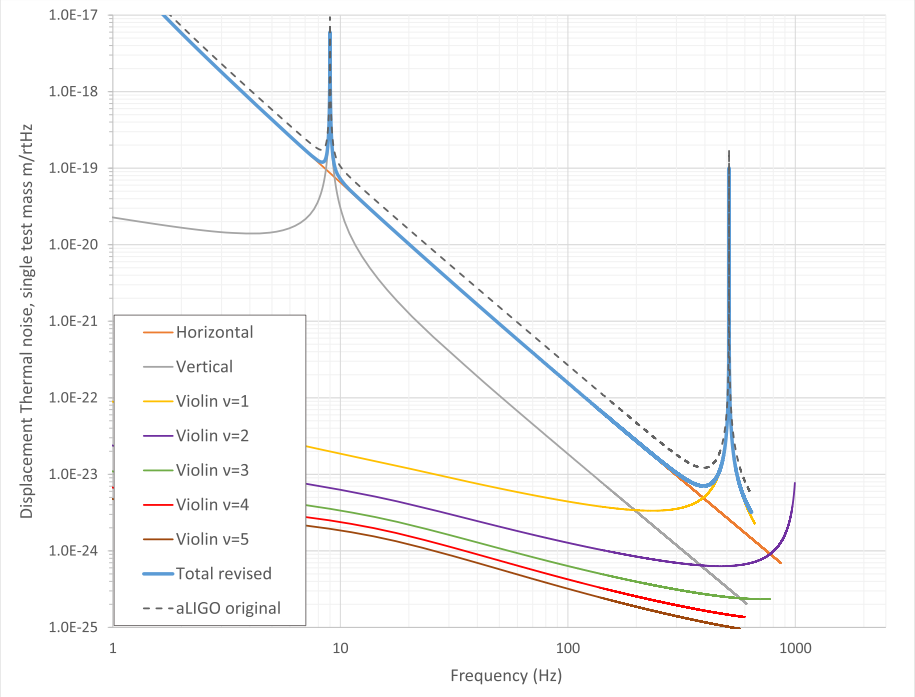

Figure 10. Displacement suspension thermal noise (single mass) re-calculated for the new estimated surface and weld loss parameters for aLIGO.

by 36% for surface loss, and 27% for weld loss respectively. This is significant as the resulting suspension thermal noise will therefore be lower (and therefore improved) over previous estimations, as shall be discussed in section 6.

In reality, both surface loss and weld loss will have non-zero contribution to the total loss of the system. Thus, the actual values of each will both be lower than the upper limits of $h\phi_s = 3.9 \times 10^{-12}$ m and $\phi_{\rm weld} = 4.2 \times 10^{-7}$ shown in figure 8, instead lying somewhere in the central region of the trough in figure 8. Therefore, we can instead consider an example of the most conservative case for the dominant loss mechanism, surface loss. This will come from the lowest experimental weld loss taken from the lowest experimental value in Heptonstall *et al* [33] of $3.2 \pm 1.8 \times 10^{-7}$, giving the lowest weld loss possible of 1.4×10^{-7} at the bound of the measurement error. Figure 9 shows the model data (in magenta) fit to the experimental data (in blue) based on the lowest experimental mechanical loss values (black crosses) used for each violin mode harmonic, when $f(h\phi_s, \phi_{\rm weld})$ is minimised for $\phi_{\rm weld} = 1.4 \times 10^{-7}$, which yields a conservative estimate for $h\phi_s$ of 2.5×10^{-12} m.

This shows that for high quality welds, contributing a small amount of dissipation to the suspension, the actual surface loss could be as much as 58% lower than the previously accepted value of 6.15×10^{-12} m. These improved values are likely to result from a number of physical reasons. Improved weld loss is likely to result from the now extremely well practiced and executed welding technique, which has been developed over the last decade, and evidenced by the high visual quality of welds (such as shown in figure 6(c)) as compared to Heptonstall *et al* [33]. Improved estimates of surface loss may result from the extended period of time that this suspension was held under vacuum. At time of measurement, the system had been

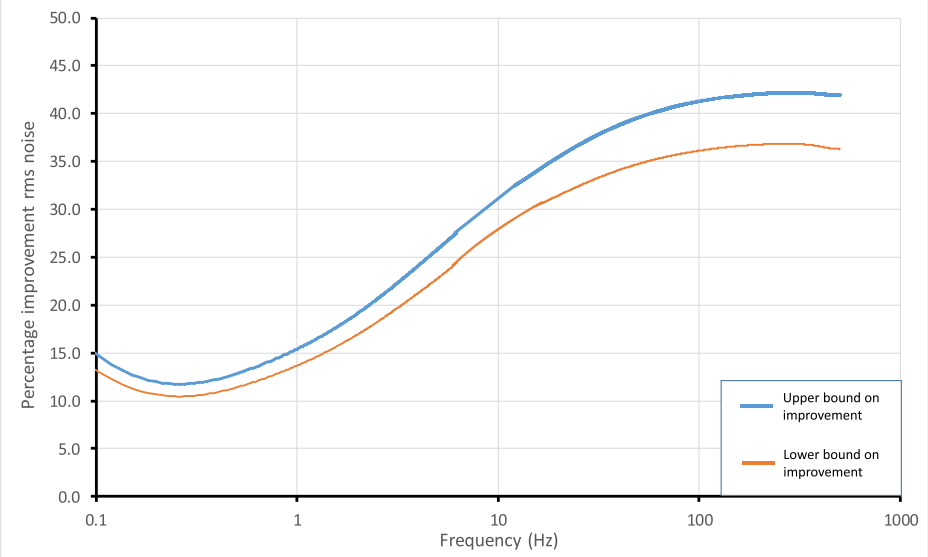

Figure 11. Range of percentage improvement in suspension thermal noise (single mass) for the new estimated surface and weld loss parameters. The curves show the upper and lower bounds based on the extreme limits for surface and weld loss discussed in section 5.

under vacuum for 17 months for the 2015 data segment and 2 months for the segment taken in 2017. This extended period under high vacuum; as compared the initial study [16] which was only under vacuum for approximately 1 month, would have allowed much of any remaining adsorbed surface water to have been pumped out of the system, with surface water known to be a contributor to higher measured losses in fused silica [35].

These results indicate that the thermal noise performance of fused silica used in interferometer end test mass suspensions will be notably superior to previous estimates, as shall now be explored.

6. Projected thermal noise re-evaluation

The total suspension thermal noise was re-calculated for each individual mode using the re-evaluated loss components evaluated in section 5. Mechanical losses for each mode are scaled appropriately from the FEA energy distributions of each respective mode. The predominant noise contribution comes from the pendulum thermal noise which is directly calculated using equation (1). Equation (3) in section 2 is used to calculate the violin modes' thermal noise, for each respective mode, and equation (12) for vertical mode thermal noise [13, 36]:

$$x_{\text{vertical}}(\omega) = 0.001\sqrt{\frac{4k_{\text{B}}T}{m\omega}\left(\frac{{\omega_{\text{vertical}}}^2\phi_{\text{vertical}}(\omega)}{{\omega_{\text{vertical}}}^4{\phi_{\text{vertical}}}^2(\omega) + \left({\omega_{\text{vertical}}}^2 - \omega^2\right)^2}\right)} \tag{12}$$

where ω_{vertical} is the respective vertical resonant mode frequency, and $\phi_{\text{vertical}}(\omega)$ is the total loss for the vertical mode, calculated again from the energy distribution of the vertical mode in FEA. The factor 0.001 is the accepted conservative estimate of vertical to horizontal motion cross coupling due to the curvature of the earth, with an additional allowance for any small

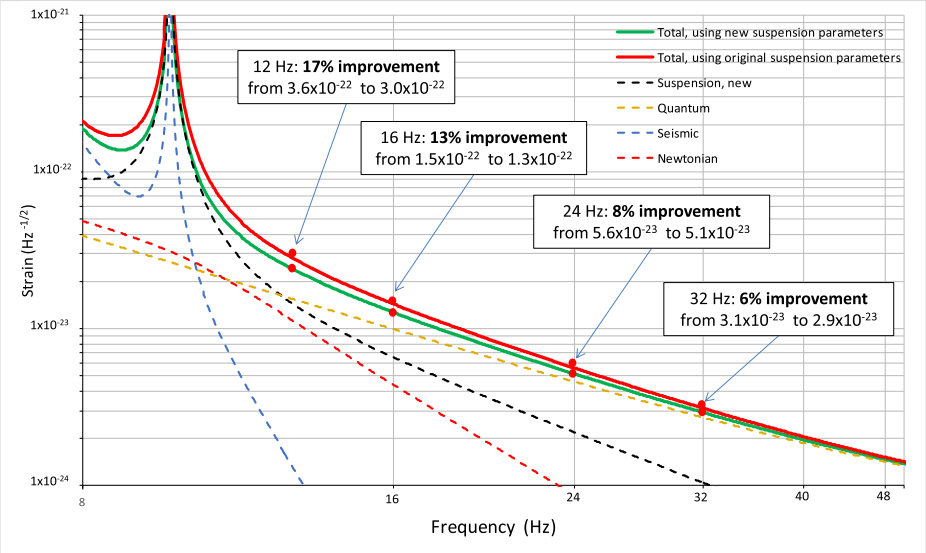

Figure 12. Improvement in low frequency A+ performance, focussed in the 8–50 Hz region, assuming modest reductions in Newtonian and quantum noise sources.

mechanical imperfections in the suspension [13]. The total noise in this modal expansion is then the quadrature sum of the individual modes noise.

In equations (1), (3) and (12), we substitute the values of $h\phi_s$, and $\phi_{\rm weld}$ from section 5 to calculate the noise directly from these revised properties of fused silica. The resulting range of potential improvement in *rms* displacement thermal noise for a single suspension is shown in figures 10 and 11. This compares the range of new weld and surface loss numbers with the original values of 6.15×10^{-12} m for $h\phi_s$ and 5.8×10^{-7} for weld loss. At 10 Hz, the projected rms thermal noise level is reduced to 6.8 to 7.4 $\times$ 10^{-20} m Hz$^{-0.5}$, which is between $\sim$27%–32% better than the value 9.5 $\times$ 10^{-20} m Hz$^{-0.5}$ calculated in reference [16]. The improvement rises to between $\sim$36%–43% at 100 Hz.

This clearly shows that the aLIGO suspension thermal noise performance is superior to that previously estimated, by a significant margin. If the drive to reduce other noise sources such as coating thermal noise is successful, such that suspension thermal noise becomes fully dominant, with an approximate average noise improvement of $\sim$30%, these new parameters lead to an increase on the estimated event rate by a factor of 2 for aLIGO.

This improved estimation of the material parameters for fused silica will be of further importance when considering the performance of future iterations of room temperature detectors. If we consider A+ [37] as an example case study of such a detector, with conservative assumed improvements of factor 1.5 to quantum noise (potentially possible with squeezing increase from 12 dB to 15.6 dB [38]) and a factor 5 to Newtonian noise (potentially possible via ongoing research into seismometer arrays [39]), tangible gains in performance are attainable with the improved suspension surface and weld loss numbers, as shown in figure 12.

Improvement in strain sensitivity performance of between 17% and 6% is seen for frequencies of $\sim$12 Hz to 32 Hz respectively. The average improvement over this frequency band is $\sim$11%, resulting in a potential improvement in event rate for A+ of $\sim$35% over this band. Additionally, for sources entering band at approximately 12 Hz, time in band will be increased by around 12% [40], yielding real astrophysical benefits, including earlier warning of binary

neutron stars entering band in this frequency region, better measurement of inspiral physics such as precession, and easier detection of high-mass sources, which merge at lower frequencies. Ultimately, if such noise sources could be further reduced, more of the full potential 30–40% improvement seen in the aLIGO curve (figure 10) could be accessed.

The reduction in surface and weld loss will also allow the design sensitivity requirements for the room temperature components of large scale silica suspensions for 3rd generation detectors, such as LIGO Cosmic Explorer and ET-HF, to be more easily achieved, and this will be subject of future publication.

7. Conclusions

Mirror suspension technologies, in particular quasi-monolithic fused silica final stage suspensions, are one of the significant enhancements installed in the current advanced generation of ground based interferometric gravitational wave observatories. This technique is now mature, and detector data has allowed the measurement of a new set of violin mode Q-factor values on individual installed suspension fibres on modes up to $\nu = 8$. These have shown the highest measured Q-factors to date—with values of up to two billion, a factor of over three higher than seen in prototype suspensions. The ultra-low level of the mechanical loss values measured has come due to the maturity of the technology in particular in the area of laser welding. These measurements allowed two of the material properties for fused silica—surface loss $h\phi_s$ and weld loss, ϕ_{weld}, to be re-evaluated. We observed a factor of between three and four improvement in these values.

Taking these parameters, it was possible to re-evaluate the full projected thermal noise of the quasi-monolithic system showing a $\sim$30% improvement compared to the prototype system at 10 Hz, and $\sim$40% improvement at 100 Hz. This leads to an increase on the estimated event rate by a factor of two, if suspension thermal noise became the main limitation to the sensitivity of the detector. These results are important for ongoing detector characterisation and the design of the suspensions of future generation gravitational wave observatories. The technique applied here is applicable to other detectors as well as future systems such as A+, which could see similar improvements if other noise sources also reduced, together with Cosmic Explorer and ET-HF, as well as future small scale laboratory experiments. Materials characterisation will remain an essential component of detector development for cryogenic detectors of the future, and the techniques shown in this publication are directly applicable to crystalline suspensions in materials, such as sapphire or silicon, going forward.

Acknowledgments

The authors would like to acknowledge our colleagues in the Institute of Gravitational Research, LIGO Scientific Collaboration, the GEO600 project, and the Scottish Universities Physics Alliance for their interest in this work. The authors would like to thank the Science and Technology Facilities Council (Grant ref: ST/N005422/1) for their financial support. The authors gratefully acknowledge the support of the United States National Science Foundation for the construction and operation of aLIGO and the LIGO laboratories. This paper has LIGO document number P2000100.

ORCID iDs

A V Cumming https://orcid.org/0000-0003-4096-7542

B Sorazu https://orcid.org/0000-0002-6178-3198
E Daw https://orcid.org/0000-0002-3780-5430
D Williams https://orcid.org/0000-0003-3772-198X

References

[1] Aasi J *et al* (Advanced LIGO) 2015 *Class. Quantum Grav.* **32** 074001
[2] Acernese F *et al* 2014 Advanced Virgo: a second-generation interferometric gravitational wave detector *Class. Quantum Grav.* **32** 024001
[3] Abbott B *et al* 2016 Observation of gravitational waves from a binary black hole Merger *Phys. Rev. Lett.* **116** 061102
[4] Abbott B *et al* 2017 GW170817: observation of gravitational waves from a binary neutron star inspiral *Phys. Rev. Lett.* **119** 161101
[5] Saulson P R 1994 *Fundamentals of Interferometric Gravitational Wave Detectors* (Singapore: World Scientific)
[6] Saulson P R 1990 Thermal noise in mechanical experiments *Phys. Rev.* D **42** 2437–45
[7] Callen H B and Welton T A 1951 Irreversibility and generalised noise *Phys. Rev.* **83** 34–40
[8] Callen H B and Greene R F 1952 On a theorem of irreversible thermodynamics *Phys. Rev.* **86** 702–10
[9] Rowan S and Hough J 2000 Gravitational wave detection by interferometry (ground and space) *Living Rev. Relativ.* **3** 3
[10] Braginsky V B *et al* 1994 On the thermal noise from the violin modes of the test mass suspension in gravitational wave antennae *Phys. Lett.* A **186** 18–20
[11] Braginsky V B *et al* 1996 Energy dissipation in the pendulum mode of the test mass suspension of a gravitational wave antenna *Phys. Lett.* A **218** 164–6
[12] Penn S D *et al* 2001 High quality factor measured in fused silica *Rev. Sci. Instrum.* **72** 3670–3
[13] Aston S M *et al* 2012 Update on quadruple suspension design for Advanced LIGO *Class. Quantum Grav.* **29** 235004
[14] Cagnoli G and Willems P 2002 Effects of nonlinear thermoelastic damping in highly stressed fibres *Phys. Rev.* B **65** 174111
[15] Willems P 2002 Dumbbell-shaped fibers for gravitational wave detectors *Phys. Lett.* A **300** 162–8
[16] Cumming A *et al* 2012 Design and development of the advanced LIGO monolithic fused silica suspension *Class. Quantum Grav.* **29** 035003
[17] Fritschel P 2002 Low-frequency cutoff for advanced LIGO *LIGO Document T020034*
[18] Cumming A *et al* 2009 Finite element modelling of the mechanical loss of silica suspension fibres for advanced gravitational wave detectors *Class. Quantum Grav.* **26** 215012
[19] McClelland D *et al* (LIGO Scientific Collaboration) 2015 Instrument science white paper (report) *LIGO Document T1500290-v2*
[20] The ET Science Team 2011 Einstein gravitational wave telescope conceptual design study ET technical document number ET-0106C-10 https://tds.ego-gw.it/itf/tds/index.php?callContent&tnqx3d;2&tnqx26;callCode&tnqx3d;8709
[21] Reitze D *et al* 2019 Cosmic explorer: the U.S. contribution to gravitational-wave astronomy beyond LIGO (arXiv:1907.04833)
[22] Brif C 1999 Notes on anelastic effects and thermal noise in suspensions of test masses in interferometric gravitational-wave detectors *LIGO Document T990041*
[23] Parks T W and Burrus C S 1987 *Digital Filter Design* (New York: Wiley)
[24] Daw E J 2020 A Bayesian adaptive filtering approach to dynamic wave tracking (unpublished)
[25] USGS 2019 Updated: Magnitude 7.1 Earthquake in Southern California (Reston, VA: United States Geological Survey) (https://www.usgs.gov/news/update-magnitude-71-earthquake-southern-california?qt-news_science_products&tnqx3d;7&tnqx23;qt-news_science_products)
[26] Gonzalez G and Saulson P R 1994 Brownian motion of a mass suspended by an anelastic wire *J. Acoust. Soc. Am.* **96** 207
[27] Cumming A 2008 Aspects of mirrors and suspensions for advanced gravitational wave detectors *PhD thesis* The University of Glasgow
[28] Cumming A *et al* 2011 Apparatus for dimensional characterization of fused silica fibers for the suspensions of advanced gravitational wave detectors *Rev. Sci. Instrum.* **82** 044502

[29] Gretarsson A and Harry G M 1999 Dissipation of mechanical energy in fused silica fibers *Rev. Sci. Instrum.* **70** 4081–7
[30] Bell C 2014 Mechanical loss of fused silica fibres for use in gravitational wave detectors *PhD thesis* The University of Glasgow
[31] Bell C *et al* 2014 Experimental results for nulling the effective thermal expansion coefficient of fused silica fibres under a static stress *Class. Quantum Grav.* **31** 065010
[32] Penn S D *et al* 2006 Frequency and surface dependence of the mechanical loss in fused silica *Phys. Lett.* A **352** 3–6
[33] Heptonstall A *et al* 2010 Investigation of mechanical dissipation in CO2 laser-drawn fused silica fibres and welds *Class. Quantum Grav.* **27** 035013
[34] Cagnoli G *et al* 2000 Damping dilution factor for a pendulum in an interferometric gravitational wave detector *Phys. Lett.* A **272** 39–45
[35] Bartenev G M, Lomovskoi V A and Sinitsyna G M 1996 Relaxation processes in silica glass *Inorg. Mater.* **32** 671–82
[36] Barton M *et al* 2008 Cavity optics suspension subsystem design requirements document *LIGO Document T010007*
[37] Barsotti L *et al* 2018 The A+ design curve *LIGO Document T1800042*
[38] Oelker E *et al* 2016 Audio-band frequency-dependent squeezing for gravitational-wave detectors *Phys. Rev. Lett.* **116** 041102
[39] Badaracco F and Harms J 2019 Optimization of seismometer arrays for the cancellation of Newtonian noise from seismic body waves *Class. Quantum Grav.* **36** 145006
[40] Hang Y *et al* 2018 Prospects for detecting gravitational waves at 5 Hz with ground-based detectors *Phys. Rev. Lett.* **120** 141102